A multi-electrode two-dimensional position sensitive diamond detector

S. Ditalia Tchernij ; D. Siciliano ; G. Provatas ; J. Forneris ✉ ; F. Picollo ; M. Campostrini ;
V. Rigato ; Z. Siketic ; M. Jaksic ; E. Vittone

Check for updates

View Online

Export Citation

13 June 2024 07:44:34

Journal of Applied Physics

Special Topic: Phase-change
Materials and Their Applications

Submit Today

AIP Publishing

AIP Publishing

A multi-electrode two-dimensional position sensitive diamond detector

View Online　　Export Citation　　CrossMark

S. Ditalia Tchernij,[1,2] (iD) D. Siciliano,[1] (iD) G. Provatas,[3] (iD) J. Forneris,[1,2,3,a)] (iD) F. Picollo,[1,2] (iD) M. Campostrini,[4] (iD)
V. Rigato,[4] (iD) Z. Siketic,[3] (iD) M. Jaksic,[3] (iD) and E. Vittone[1,2] (iD)

AFFILIATIONS

[1]Physics Department, University of Torino, Torino, Italy
[2]Istituto Nazionale di Fisica Nucleare Sez. Torino, Torino, Italy
[3]Laboratory for Ion Beam Interactions, Institut Ruder Boskovic, Zagreb, Croatia
[4]Istituto Nazionale di Fisica Nucleare, Laboratori Nazionali di Legnaro, Legnaro, Italy

[a)]Author to whom correspondence should be addressed: jacopo.forneris@unito.it

ABSTRACT

In multi-electrode devices, charge pulses at all the electrodes are induced concurrently by the motion of the excess charge carriers generated by a single ion. This charge-sharing effect is such that the pulse amplitude at each sensitive electrode depends on the device geometry, its overall electrostatic configuration, and the charge transport properties of the detecting material. Therefore, the cross-analysis of the charge pulses induced at each electrode offers implicit information on the position of the ion impact. In this work, we investigate the two-dimensional position sensitivity of a diamond detector fabricated by deep ion beam lithography. By exploiting the ion beam induced charge technique, the device was exposed to a 2 MeV Li$^+$ ion micro-beam to map the spatial dependence of the charge collection efficiency (CCE) on the nominal micro-beam scanning position. The combination of the CCE maps revealed a two-dimensional position sensitivity of the device with micrometric resolution at the center of the active region.

Ion beams are consolidated tools for the characterization and functionalization of materials and electronic devices and detectors and are commonly adopted for materials manufacturing processes.[1–3] The availability of dedicated setups for the delivery of focused or collimated ion beams with sub-micrometer resolution[4–7] has enabled the flourishing of spatial-resolved experimental techniques for the characterization of the charge transport properties of detectors and semiconductors,[8,9] the effects of radiation damage on their response,[10–13] and the analysis of single event effects in microelectronic devices.[14,15] Conversely, the availability of real-time position-sensitive single-ion detectors could enable the controlled dose delivery at the micrometric scale for the assessment of radiation damage at high doses,[16] the selective functionalization of materials,[17,18] or the implementation of cell culture irradiation protocols for micro-radiobiology experiments.[19,20] It would also enable to obtain high spatial sensitivity on individual ion strike position without the need for focusing or collimating ion optics elements.

Recent works have explored the possibility to exploit the implantation targets themselves as resources for position-sensitive single-ion detection.[21–23] Particularly, the exploitation of charge-sharing effects in multi-electrode devices to both sense the impact of individual keV and MeV ions in solid state detectors and concurrently retrieve their impinging position has been proposed.[24–26] Specifically, it was shown that the evaluation of the induced charge shared between multiple electrodes could be used to detect the ion strike location with sub-micrometer precision. Despite the premises, these results were, however, based on simple one-dimensional geometries and offered a limited (i.e., few μm) position-sensitive detection regions. In this work, we present a proof-of-concept experiment based on the ion beam induced charge (IBIC)[27] technique to determine the ion beam impact point position of a MeV ion. The methodology requires initially the acquisition of charge collection efficiency (CCE) maps by three sensitive detectors located at the vertices of an equilateral triangle, which is the active area probed by a scanning focused MeV ion beam. The measurements of the charges induced at the three sensing electrodes by a MeV ion impacting the active area, combined with the three CCE maps, enable the identification of the impact position of a MeV ion with the same mass and energy with a resolution at the micrometer scale. The detector was fabricated on a commercial $3 \times 3 \times 0.3$ mm^3

13 June 2024 07:44:34

synthetic single-crystal diamond substrate by Element Six ($\langle 100 \rangle$ orientation). The sample was denoted as "electronic grade" according to the low contents of substitutional N and B impurities (<5 ppb). The device consists of a sandwich geometry in which the top side is segmented into three independent sensing electrodes. The three top electrodes are buried graphitic micro-channels fabricated according to the high-resolution deep ion beam lithography (DIBL) technique[19,28] summarized in Figs. 1(a) and 1(b). A 3 μm thick Cu layer was thermally evaporated on the substrate surface [Fig. 1(b)] and was subsequently micromachined by FIB milling (30 keV Ga$^+$ ions) in order to define a lithographic mask for broad ion beam lithography [SEM image in Fig. 1(a)]. The apertures enabled to selectively amorphize the regions patterned by the mask by exposing the diamond substrate to an unfocussed (3 $\times$ 3 mm^2 spot size) 4 MeV C^{3+} ion beam. The ion fluence ($\sim 2.5 \times 10^{16}$ cm^{-2}) was set to introduce a vacancy density above the diamond graphitization threshold (9×10^{22} cm^{-3})[29] at the end of the ion range, thus resulting in the formation of conductive graphitic electrodes upon high-temperature post-irradiation thermal annealing (1000 °C, 2 h, 5×10^{-5} mbar). The selected ion energy resulted in the fabrication of ~ 1 μm thick graphitic electrodes located at 1.5 μm depth from the diamond surface, according to SRIM simulations[30] [Fig. 1(c)]. The choice of the fabrication of electrodes buried below the sample surface, while not strictly necessary for the operation of a detector based on the charge-sharing effect, was made to ensure the formation of Ohmic contacts,[31,32] as well as to mitigate the electrostatic effects induced by the surface termination.

The utilization of a FIB for the preparation of a contact lithographic mask [Fig. 1(a)] enabled to achieve the fabrication of graphitic structures with a spatial resolution limited only by the lateral straggling of the 4 MeV C^{3+} ions in diamond (~ 100 nm[30]) and in copper due to surface scattering of carbon ions with the copper vertical walls, due to

the beam divergence and slight misalignment of beam with respect to the mask (~ 350 nm). This prevented the introduction of radiation induced defects in the active region of the detector,[33] which could hinder the electrical and detection properties of the device. The choice of a C ion beam was made both to avoid the introduction of external atomic species in the diamond lattice, involving the formation of additional electrically active defects,[34] and to define buried structures in which the μm-deep electron–hole cloud generated by impinging MeV ions in IBIC experiments can be regarded as described by a purely planar geometry.

The resulting device consisted of three 5 μm wide, 75 μm long [Fig. 2(a)] buried graphitic electrodes placed at a relative angle of 120°. Their inner endpoints defined the vertices of an equilateral triangle with a side of 26 μm. Their outer endpoints were FIB milled and then connected to the external biasing circuitry by means of 50 nm thick Al electrodes, deposited by electron beam lithography and subsequently wire bonded to an external custom sample holder.[29] Finally, an additional 50 nm thick Al electrode was deposited on the back side of the diamond sample, i.e., on the surface opposite to the graphitic buried electrode.

The device was characterized by ion beam induced charge (IBIC) microscopy, enabling to record the pulse height, associated with the charge induced by the motion of electrons and holes generated by individual ions, with the nominal position of incidence of a rarefied MeV ion microbeam raster scanning on the sample surface.[27]

The device was arranged according to the electrostatic configuration depicted in Fig. 2(a). Each of the three planar electrodes (named R, G, and B) was connected to an independent charge-sensitive electronic chain, consisting of a Amptek A250 preamplifier[35] and a ORTEC model 570 shaping amplifier. The induced charge pulses associated with the detection of individual ions were then digitized using a
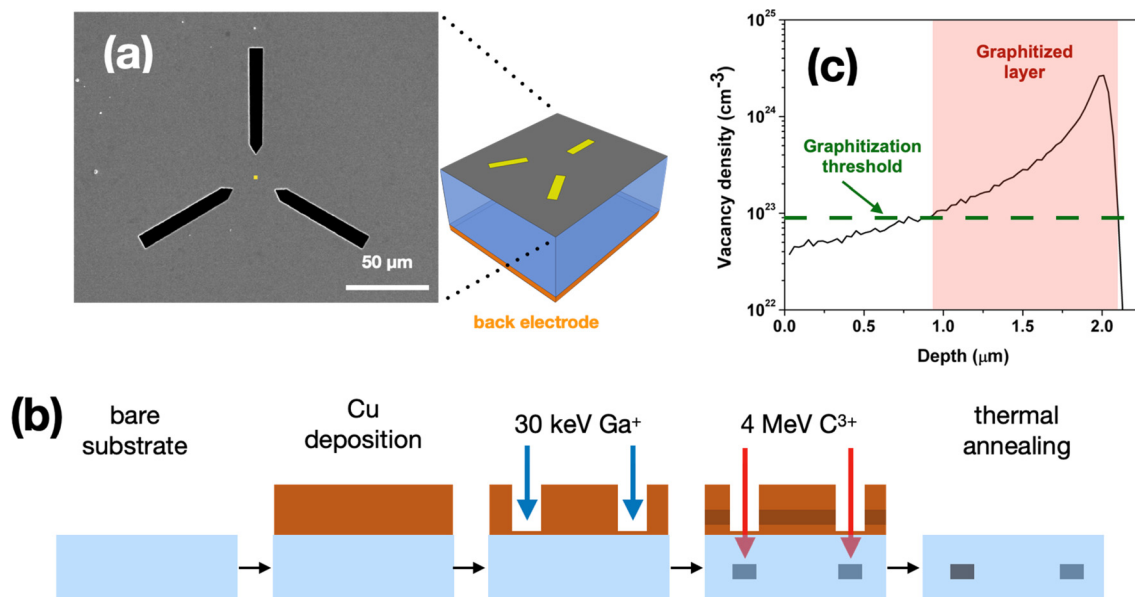
FIG. 1. (a) Scanning electron microscopy (SEM) image of the lithography mask adopted for the fabrication of the segmented top electrode of the detector. The three planar electrodes are placed about 1.5 μm beneath the top surface of a diamond plate and biased with respect to a reference electrode on the back surface. (b) Sketch of the fabrication steps implemented for the deep ion beam lithography process. (c) Vacancy density profile for 4 MeV C^{3+} ions in diamond, according to SRIM simulations.[30]
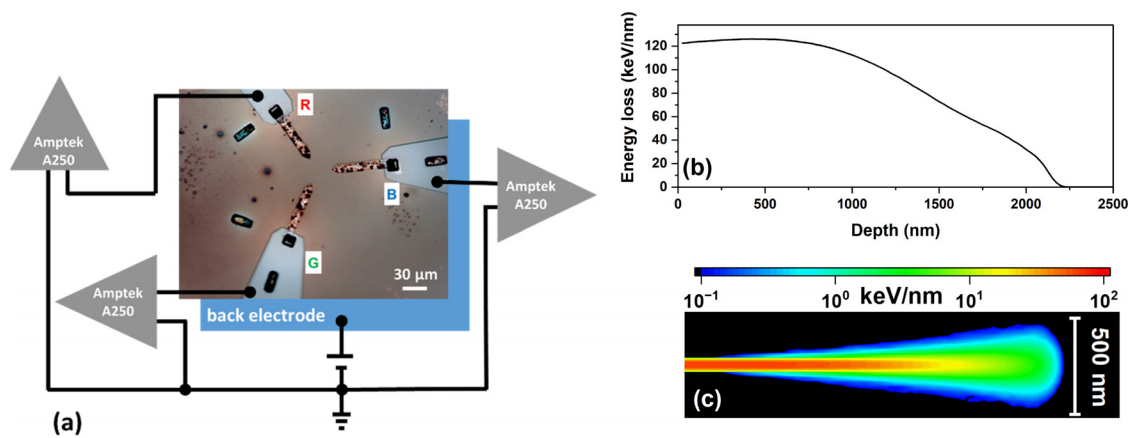
FIG. 2. (a) Optical micrograph of the diamond detector with ion-beam-micromachined graphitic electrodes (top surface). The back electrode is sketched in the figure together with the electrical connections adopted for the IBIC experiment. (b) Ionization profile and (c) contour plot of the energy loss for 2 MeV Li$^+$ ions in diamond as evaluated by SRIM simulations.

multi-channel analyzer interfaced with the SPECTOR software.[36] The three electrodes were virtually grounded through the preamplifiers, and the back electrode was held at a constant applied voltage of 60 V with respect to a common ground.

A 2 MeV Li$^+$ beam was chosen as the probing beam; the ionization energy loss profile and the 2D contour plot are shown in Figs. 2(b) and 2(c), respectively. Although the ionization profile is not optimal to maximize the induced charge collection (at 1500 nm the energy
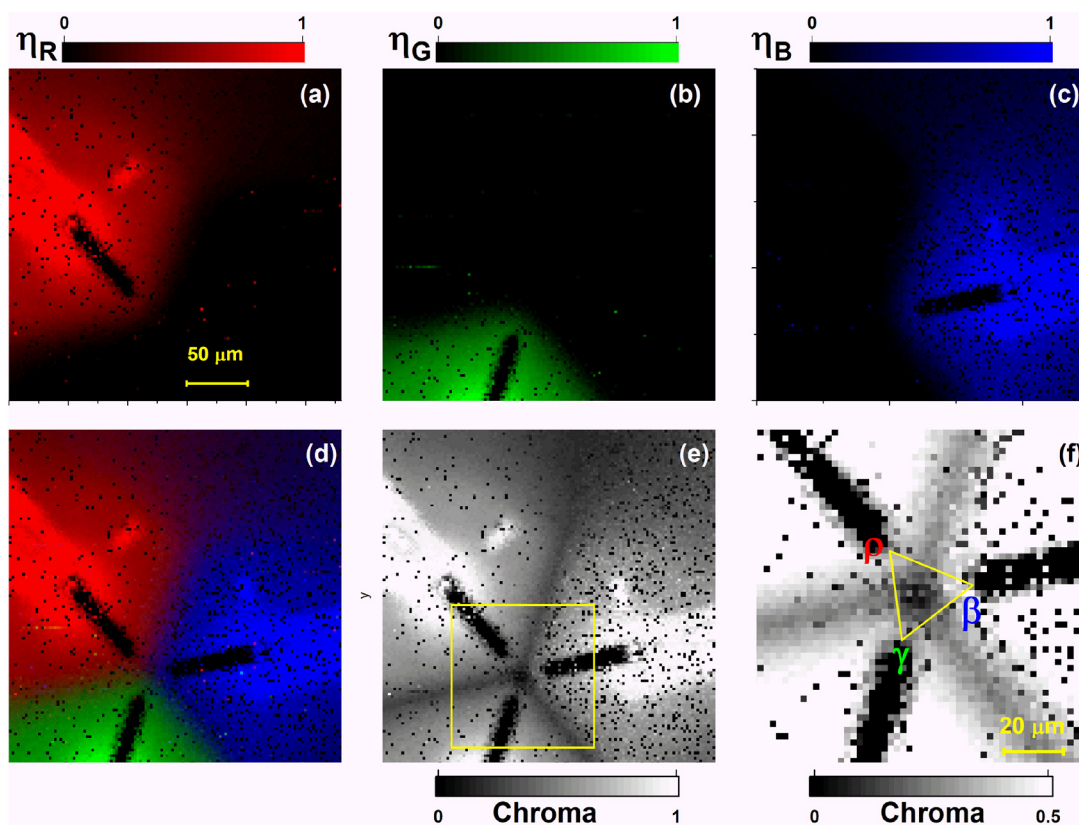
FIG. 3. (a)–(c) Median maps of the charge collection efficiency η measured by each of the three sensing electrodes [R, G, and B, as labeled in Fig. 2(a)] upon raster scanning of a rarefied 2 MeV Li+ beam. (d) The RGB-encoded IBIC map resulting from the combination of the three previous maps. (e) Chroma map encoded as a grayscale image. (f) Chroma-encoded map zoom-in the yellow square of (e). The equilateral triangle (side 26 μm) is the region of interest analyzed in Fig. 4.
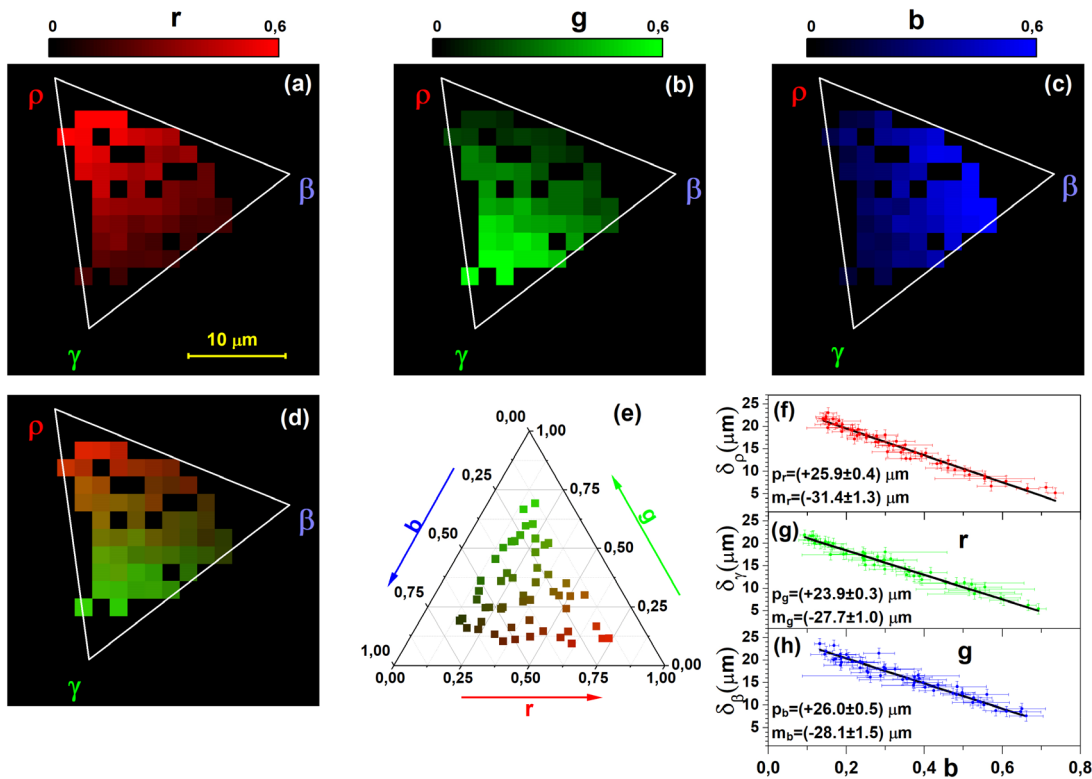
FIG. 4. (a)–(c) Median maps of the normalized charge collection efficiency r, g, b measured by each of the three sensing electrodes, restricted to the pixels for which all the three values have non-zero values. (d) The RGB-encoded IBIC map resulting from the combination of the three previous maps. (e) Maxwell triangle of color, representing the three coordinates in the "charge space" of the pixels shown in (d). (f) Plot of the distance (δ_ρ) from the ρ vertex as function of the "r" normalized charge collection efficiency; (g) plot of the distance (δ_γ) from the γ vertex as a function of the "g" normalized charge collection efficiency; and (h) plot of the distance (δ_β) from the β vertex as a function of the "b" normalized charge collection efficiency. In the last three graphs, the lines are the linear fit calculated by using the algorithm of Fasano and Vio;[39] $p_{r,g,b}$ and $m_{r,g,b}$ are the resulting intercept and slope, respectively. The horizontal and vertical error bars are given by the interquartile range of the pulse distribution in each pixel and the FWHM of the beam spot, respectively.

loss is approximately half than at 500 nm), diffusion (the diffusion length is larger than 1 μm), and drift because the bending of the electric field at the surface is effective to drive carriers along trajectories traversing the weighting potential region (as demonstrated by simulations reported in the supplementary material), making 2 MeV Li$^+$ ions effective to probe the induced charge in the sensitive region.

On the basis of this arrangement, the device is to be regarded as a segmented detector with a planar geometry with respect to holes,
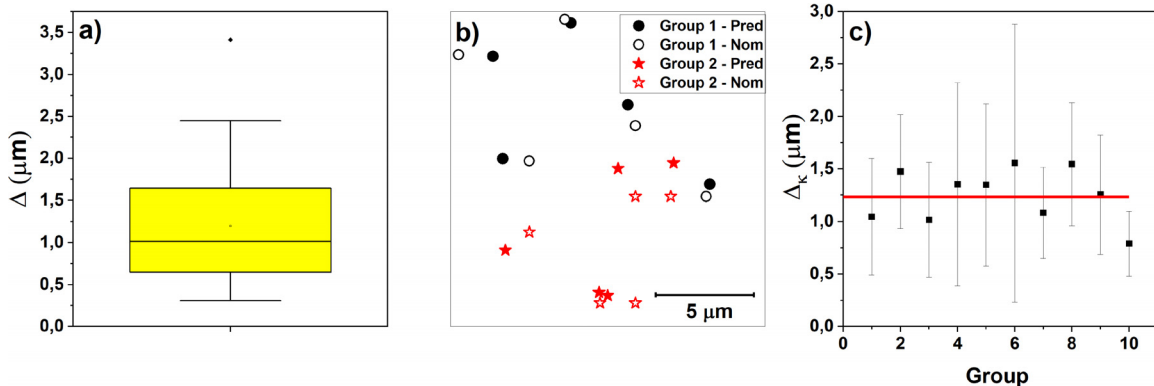
FIG. 5. (a) Box plot of the distribution of the distance from the predicted point and the nominal impact point. (b) Scatterplot of the predicted (full markers) and nominal impact points relevant to the first two groups of the cross-validation test. (c) Average distance from the predicted to the nominal point positions relevant to the ten groups. Error bars are the standard deviations.

whose collection occurs at each of the three top graphitic electrodes [Fig. 1(a)]. Conversely, electrons drift toward the back surface.

The beam spot size of the beam focused by a quadrupole triplet was estimated as (2.3 ± 0.6) μm, according to a preliminary STIM characterization.[13]

The active region of the devices was mapped using a rarefied (<100 ions/s) ion beam, by the concurrent measurement of the charge collection efficiency η_i, $i = $ R, G, B relevant to each individual sensing electrode. The analysis was performed on the maps by treating the signals as independent, i.e., the signals were not acquired under coincidence conditions.

The IBIC maps acquired from each sensing electrode under the afore-mentioned electrical bias conditions are reported in Figs. 3(a) and 3(c), where the brightness of the color scales encodes the median η_i (minimum two events recorded per pixel) value acquired at each pixel. The highest signals occur at the Al electrode connecting the graphitic channel endpoints, and the collection efficiency refers to this value.

In correspondence of the graphitic electrodes, the CCE is lower than the noise threshold as a result of immediate trapping of the electron–hole pairs generated by the impinging ions in a highly defective, radiation-damaged region as a consequence of the deep ion beam lithography process.

Figure 3(d) is the RGB-encoded IBIC map resulting from the combination of the three maps [Figs. 3(a) and 3(c)]. This representation introduces the possibility of using other colorimetric quantities, which enables the highlighting of specific features, which are functional to the development of a position sensitive detector (PSD). Actually, the chroma (the absolute value of color purity, i.e., [Max(η_R, η_G, η_B) − min(η_R, η_G, η_B)])[37] encoded IBIC map [Fig. 3(e)] exhibits a snowflake's sixfold symmetry: three of the arms are the (black) graphitic channels and the remaining three (grey) main arms correspond to the regions where charge sharing occurs between two adjacent electrodes. These latter converge into the central region, which corresponds to the minimum of chroma, as shown in the zoomed map in Fig. 3(f), relevant to the yellow square in Fig. 3(e).

The equilateral triangle with the vertices (named ρ, γ, β) of the graphitic channels shown in Fig. 3(f), defines the region of interest for the PSD (about 293 μm^2), where the three electrodes share the charge signals.

Actually, pixels for which non-zero η values were recorded at all the three sensing electrodes, lie within the equilateral triangle as shown in Figs. 4(a)–4(c), where the color scale encodes the new normalized coordinates $r = \frac{\eta_R}{(\eta_R + \eta_G + \eta_B)}$; $g = \frac{\eta_G}{(\eta_R + \eta_G + \eta_B)}$; $b = \frac{\eta_B}{(\eta_R + \eta_G + \eta_B)}$ and in the RGB-encoded IBIC map in Fig. 4(d).

The adoption of these normalized new variables allows the representation of the three induced signals in a new "charge space," represented by a ternary diagram [Fig. 4(e)], which is nothing but the Maxwell's triangle of colors,[38] in which a given plotted point represents the relative proportions of three variables, constrained by r + g + b = 1.

The localization of the ion impact position can therefore be traced back to the search for the one-to-one correspondence (bijective function), which maps each point within the region of interest ROI [the equilateral triangle $\rho\gamma\beta$ shown in Fig. 4(f)] to one relevant point, identified by the normalized coordinates (r, g, b), in the "charge space." This bijective function can be found by observing that in Figs. 4(a)–4(c), the intensity of each primary color decreases radially from the reference vertex of the equilateral triangle. The dependence of the radial distance δ_ρ of the impact points with coordinates (x_{nom}, y_{nom}) (given by the microbeam scanner) from the vertex (x_ρ, y_ρ) of the electrode "R," i.e.,

$$\delta_\rho = \sqrt{(x_{nom} - x_\rho)^2 + (y_{nom} - y_\rho)^2}, \quad (1)$$

as function of the "charge coordinate r" relevant to that electrode, is shown in Fig. 4(f). Similarly, Figs. 4(g) and 4(h) show similar graphs to the distances δ_γ and δ_β of the impact points (x_{nom}, y_{nom}) from the vertices (x_γ, y_γ) and (x_β, y_β) relevant to the electrodes G and B, respectively. These linear trends are, at least qualitatively, in agreement with the IBIC theory,[40] as can be seen from the simulations described in the supplementary material.

The resulting graphs show linear decreasing behaviors, such that the bijective function turns out to be a linear transformation,

$$\begin{cases} \delta_\rho = p_r + m_r \cdot r, \\ \delta_\gamma = p_g + m_g \cdot g, \\ \delta_\beta = p_b + m_b \cdot b, \end{cases} \quad (2)$$

where $p_{r,g,b}$ and $m_{r,g,b}$ are the intercepts and the slopes of the linear regressions, calculated using the algorithm proposed by Fasano and Vio,[39] in order to take into account both the uncertainty of the beam position (2.3 μm as evaluated from STIM mapping[13]) and the uncertainty of the normalized charge coordinates calculated from the interquartile range of the pulse distribution in each pixel (in average, 4.5 pulses per pixel).

The (x_{pred}, y_{pred}) coordinates of the predicted impact point are then calculated by solving the system (2),

$$x_{pred} = +\frac{1}{2} \frac{y_\beta\left(\delta_\rho^2 - x_\rho^2 - y_\rho^2 - \delta_\gamma^2 + x_\gamma^2 + y_\gamma^2\right) + y_\gamma\left(\delta_\beta^2 - x_\beta^2 - y_\beta^2 - \delta_\rho^2 + x_\rho^2 + y_\rho^2\right) + y_\rho\left(\delta_\gamma^2 - x_\gamma^2 - y_\gamma^2 - \delta_\beta^2 + x_\beta^2 + y_\beta^2\right)}{(y_\beta - y_\rho)(x_\gamma - x_\rho) - (x_\beta - x_\rho)(y_\gamma - y_\rho)},$$

$$y_{pred} = -\frac{1}{2} \frac{x_\beta\left(\delta_\rho^2 - x_\rho^2 - y_\rho^2 - \delta_\gamma^2 + x_\gamma^2 + y_\gamma^2\right) + x_\gamma\left(\delta_\beta^2 - x_\beta^2 - y_\beta^2 - \delta_\rho^2 + x_\rho^2 + y_\rho^2\right) + x_\rho\left(\delta_\gamma^2 - x_\gamma^2 - y_\gamma^2 - \delta_\beta^2 + x_\beta^2 + y_\beta^2\right)}{(y_\beta - y_\rho)(x_\gamma - x_\rho) - (x_\beta - x_\rho)(y_\gamma - y_\rho)}. \quad (3)$$

Figure 5(a) shows the boxplot of the distribution distances Δ_i of the nominal impact point position from the predicted impact point,

$$\Delta_i = \sqrt{(x_{pred,i} - x_{nom,i})^2 + (y_{pred,i} - y_{nom,i})^2}. \quad (4)$$

The mean value is 1.2 μm, with an interquartile distance of about 1 μm.

The trilateration procedure summarized above is thus equivalent to the identification of the single intersection point between three circumferences.

To measure the predictive accuracy of the model, we used a ten-fold cross validation test.[41] The 52 data points were randomly assigned to ten groups, containing five points identified by the three "charge" coordinates (ρ, γ, β) relevant to the nominal point of coordinates (x_{nom}, y_{nom}). In turns, the remaining 47 points were used to build the above described model to evaluate the predicted impact point (x_{pred}, y_{pred}) through Eqs. (1)–(3). As an example, Fig. 5(b) shows the scatterplot of the nominal and predicted impact point positions relevant to the first two groups. The accuracy of the model was quantified by the mean and standard deviation of the distance Δ_k defined in (4) relevant to the kth group as shown in the scatterplot in Fig. 5(c). The resulting average value agrees with the mean value evaluated from the whole data set shown in Fig. 5(a). The accuracy of the impact ion position can finally be determined by combining in quadrature the average Δ value with the ion beam spot size, as determined by STIM,[13] resulting in about 3.0 μm.

In conclusion, we have fabricated a multielectrode diamond detector by means of deep ion beam lithography, both satisfying the requirement of bias-independent internal space charge density and being a material of interest for the delivery of individual ions. The detector was characterized by mapping the CCE relevant to each sensitive electrode biased with respect to a reference metallic back electrode. The induced charge relevant to the ion impact within the region of interest delimited by an equilateral triangle with the vertices at the endpoints of the electrodes, was found to be shared between the three electrodes, with an efficiency which linearly decreases as a function of the distance of the impact point from the electrodes tips. This latter evidence allowed the coordinate and the charge spaces to be correlated and enabled to apply simple algorithms to identify the position of impact of individual ions in the inter-electrode region of the detector, where charge-sharing events were recorded. The proposed trilateration approach has demonstrated the potential to retrieve the two-dimensional position of impact of each ion with a spatial uncertainty of 3 μm over a triangular region with 26 μm side.

The results obtained by this proof-of-concept methodology can be substantially enhanced both by implementing incremental improvements in the experimental setup and by considering alternative device designs. The spatial resolution is expected to result from a convolution between the probing ion beam spot size and the uncertainty budget in the determination of the median charge collection efficiency value from an individual pixel of the IBIC maps. The adoption of coincidence detection from all the electrodes will enable the identification of the position of individual ion from an impinging broad beam. The intrinsic resolution of the detector can therefore be enhanced by a calibration performed taking advantage of focused or collimated ion beams with sub-μm spot size.[42] Furthermore, the utilization of dedicated low-noise preamplifiers for the detection of induced charge pulses[23,35] will lead to a dramatic decrease in the uncertainty affecting the charge collection efficiency, thus enabling the acquisition of more accurate charts relating the induced charges space with that of the two-dimensional spatial coordinates, as well as in the achievement of high-resolution for lower energy experiments.[23] The currently achieved position sensitivity of 3 μm corresponds to a CCE variation of $\sim$0.1 along the radial distance from each electrode, and thus to a minimum

energy resolution of 200 keV. This observation enables to anticipate the direct implementation of the proposed methods for single-ion position-sensitive detection in experiments with energies of few hundreds of keV.[43] Also, alternative electrode arrangements and the shrinking of the electrode spacing can lead to significant improvement in the spatial resolution. Based on these perspectives, the proposed methodology could become an effective method for the development of deterministic doping process with real-time feedback both on the delivery of individual ions, due to the single-ion sensitivity of the IBIC technique, and on their position sensitivity. This technique might thus find application for dopants engineering in quantum technologies,[44–47] offering the development of devices the same electrodes exploited for deterministic ion placement can be subsequently exploited to drive and control the properties of the fabricated individual dopants.[44–50]

See the supplementary material for the results of a finite element simulation describing the IBIC experiment on the basis of the electrostatic analysis of the device and the implementation of the Shockley–Ramo–Gunn theory.

AUTHOR DECLARATIONS
Conflict of Interest

The authors have no conflicts to disclose.

Author Contributions

S. Ditalia Tchernij: Formal analysis (equal); Resources (equal); Writing – review & editing (equal). **D. Siciliano:** Formal analysis (equal); Investigation (equal); Validation (equal); Writing – review & editing (equal). **G. Provatas:** Data curation (equal); Investigation (equal); Writing – review & editing (equal). **J. Forneris:** Conceptualization (lead); Formal analysis (equal); Funding acquisition (equal); Investigation (equal); Methodology (lead); Writing – original draft (equal). **F. Picollo:** Methodology (equal); Resources (equal); Validation (equal); Writing – review & editing (equal). **M. Campostrini:** Formal analysis (equal); Resources (equal); Writing – review & editing (equal). **V. Rigato:** Funding acquisition (equal); Methodology (equal); Writing – review & editing (equal). **Z. Siketić:** Funding acquisition (equal); Investigation (equal); Project administration (equal); Resources (equal); Supervision (equal); Writing – review & editing (equal). **M. Jaksic:** Data curation (equal); Project administration (equal); Resources (equal); Supervision (equal); Writing – review &

editing (equal). **E. Vittone:** Conceptualization (equal); Data curation (lead); Formal analysis (equal); Investigation (equal); Visualization (lead); Writing – original draft (equal).

DATA AVAILABILITY

The data that support the findings of this study are available from the corresponding author upon reasonable request.

REFERENCES

[1]Z. Li and C. Feng, "Ion beam modification of two-dimensional materials: Characterization, properties, and applications," Appl. Phys. Rev. **4**, 011103 (2017).

[2]F. Watt, M. B. Breese, A. A. Bettiol et al., "Proton beam writing," Mater. Today **10**, 20 (2007).

[3]W. Li, X. Zhan, X. Song et al., "A review of recent applications of ion beam techniques on nanomaterial surface modification: Design of nanostructures and energy harvesting," Small **15**, 1901820 (2019).

[4]A. G. Ponomarev and A. A. Ponomarov, "Beam optics in nuclear microprobe: A review," Nucl. Instrum. Methods Phys. Res., Sect. B **497**, 15–23 (2021).

[5]X. Xu, R. Pang, P. Santhana Raman et al., "Fabrication and development of high brightness nano-aperture ion source," Microelectron. Eng. **174**, 20–23 (2017).

[6]C. Scheuner, S. Jankuhn, J. Vogt et al., "Nanometer collimation enhancement of ion beams using channeling effects in track-etched mica capillaries," Sci. Rep. **7**, 17081 (2017).

[7]N. Raatz, C. Scheuner, S. Pezzagna et al., "Investigation of ion channeling and scattering for single-ion implantation with high spatial resolution," Phys. Status Solidi A **216**(21), 1900528 (2019).

[8]M. Girolami, G. Conte, D. M. Trucchi et al., "Investigation with β-particles and protons of buried graphite pillars in single-crystal CVD diamond," Diamond Relat. Mater. **84**, 1–10 (2018).

[9]Z. Pastuovic, J. Davis, T. L. Tran et al., "IBIC microscopy—The powerful tool for testing micron – Sized sensitive volumes in segmented radiation detectors used in synchrotron microbeam radiation and hadron therapies," Nucl. Instrum. Methods Phys. Res., Sect. B **458**, 90–96 (2019).

[10]D. Bachiller-Perea, J. Garcia Lopez, M. Jimenez-Ramos et al., "Characterization of the charge collection efficiency in silicon 3-D-detectors for microdosimetry," IEEE Trans. Instrum. Meas. **70**, 6005211 (2021).

[11]E. Vittone, Z. Pastuovic, M. B. H. Breese et al., "Charge collection efficiency degradation induced by MeV ions in semiconductor devices: Model and experiment," Nucl. Instrum. Methods Phys. Res., Sect. B **372**, 128–142 (2016).

[12]J. Garcia Lopez, M. C. Jimenez-Ramos, M. Rodriguez-Ramos et al., "An upgraded drift-diffusion model for evaluating the carrier lifetimes in radiation-damaged semiconductor detectors," Nucl. Instrum. Methods Phys. Res., Sect. B **371**, 294–297 (2016).

[13]G. Andrini, E. Nieto Hernandez, G. Provatas et al., "An ion beam spot size monitor based on a nano-machined Si photodiode probed by means of the ion beam induced charge technique," Vacuum **205**, 111392 (2022).

[14]A. M. Tonigan, D. J. Ball, G. Vizkelethy et al., "Impact of surface recombination on single-event charge collection in an SOI technology," IEEE Trans. Nucl. Sci. **68**, 305–311 (2021).

[15]V. A. Pan, J. Vohradsky, B. James et al., "Application of an SOI microdosimeter for monitoring of neutrons in various mixed radiation field environments," IEEE Trans. Nucl. Sci. **69**, 491–500 (2022).

[16]E. Vittone, J. Garcia Lopez, M. Jakšić et al., "Determination of radiation hardness of silicon diodes," Nucl. Instrum. Methods Phys. Res., Sect. B **449**, 6–10 (2019).

[17]S. Azimi, Z. Y. Dang, K. Ansari et al., "Fabrication of silicon molds with multi-level, non-planar, micro- and nano-scale features," Nanotechnology **25**, 375301 (2014).

[18]S. Lagomarsino, P. Olivero, F. Bosia et al., "Evidence of light guiding in ion-implanted diamond," Phys. Rev. Lett. **105**(23), 233903 (2010).

[19]F. Picollo, G. Tomagra, V. Bonino et al., "Triggering neurotransmitters secretion from single cells by x-ray nanobeam irradiation," Nano Lett. **20**, 3889–3894 (2020).

[20]G. Tomagra, G. Peroni, P. Aprà et al., "Diamond-based sensors for in vitro cellular radiobiology: Simultaneous detection of cell exocytic activity and ionizing radiation," Biosens. Bioelectron. **220**, 114876 (2023).

[21]M. Jakšić, Z. Medunic, M. Bogovac, and N. Skukan, "Radiation damage microstructures in silicon and application in position sensitive charged particle detection," Nucl. Instrum. Methods Phys. Res., Sect. B **231**, 502–506 (2005).

[22]J. B. S. Abraham, B. A. Aguirre, J. L. Pacheco et al., "Fabrication and characterization of a co-planar detector in diamond for low energy single ion implantation," Appl. Phys. Lett **109**(6), 063502 (2016).

[23]A. M. Jakob, S. G. Robson, V. Schmitt et al., "Deterministic shallow dopant implantation in silicon with detection confidence upper-bound to 99.85% by ion–solid interactions," Adv. Mater. **34**, 2103235 (2022).

[24]L. M. Jong, J. N. Newnham, C. Yang et al., "Charge sharing in multi-electrode devices for deterministic doping studied by IBIC," Nucl. Instrum. Methods Phys. Res., Sect. B **269**, 2336–2339 (2011).

[25]J. Forneris, D. N. Jamieson, G. Giacomini et al., "Modeling of ion beam induced charge sharing experiments for the design of high resolution position sensitive detectors," Nucl. Instrum. Methods Phys. Res., Sect. B **306**, 169–175 (2013).

[26]D. N. Jamieson, C. Yang, T. Hopf et al., "Controlled shallow single-ion implantation in silicon using an active substrate for sub-20-keV ions," Appl. Phys. Lett. **86**, 202101 (2007).

[27]E. Vittone, Z. Pastuovic, P. Olivero et al., "Semiconductor characterization by scanning ion beam induced charge (IBIC) microscopy," Nucl. Instrum. Methods Phys. Res., Sect. B **266**, 1312–1318 (2008).

[28]F. Picollo, A. Battiato, E. Bernardi et al., "Realization of a diamond based high density multi electrode array by means of Deep Ion Beam Lithography," Nucl. Instrum. Methods Phys. Res., Sect. B **348**, 199–202 (2015).

[29]S. Ditalia Tchernij, N. Skukan, F. Picollo et al., "Electrical characterization of a graphite-diamond-graphite junction fabricated by MeV carbon implantation," Diamond Relat. Mater. **74**, 125–131 (2017).

[30]J. F. Ziegler, M. D. Ziegler, and J. P. Biersack, "SRIM—The stopping and range of ions in matter," Nucl. Instrum. Methods Phys. Res., Sect. B **268**, 1818–1823 (2010).

[31]S. Koizumi, K. Watanabe, M. Hasegawa et al., "Formation diamond p–n junction its optical emission characteristics," Diamond Relat. Mater. **11**, 307–311 (2002).

[32]T. Matsumoto, H. Kato, N. Tokuda et al., "Reduction of n-type diamond contact resistance by graphite electrode," Phys. Status Solidi RRL **8**, 137–140 (2014).

[33]J. Forneris, S. Ditalia Tchernij, P. Traina et al., "Mapping local spatial charge defective diamond by means N-V sensors—A self-diagnostic concept," Phys. Rev. Appl. **10**(1), 014024 (2018).

[34]G. Prestopino, M. Marinelli, E. Milani et al., "Photo-physical properties of He-related color centers in diamond," Appl. Phys. Lett. **111**(11), 111105 (2017).

[35]E. C. Auden, B. L. Doyle, E. Bielejec et al., "Optimization of a low noise detection circuit for probing the structure of damage cascades with IBIC," Phys. Procedia **66**, 561–567 (2015).

[36]D. Cosic, M. Bogovac, and M. Jakšić, "Data acquisition and control system for an evolving nuclear microprobe," Nucl. Instrum. Methods Phys. Res., Sect. B **451**, 122–126 (2019).

[37]A. R. Smith, "Color gamut transform pairs," Comput. Graph. **12**, 12–19 (1978).

[38]M. S. Longair, "Maxwell and the science of colour," Philos. Trans. R. Soc., A **366**, 1685–1696 (2008).

[39]G. Fasano and R. Vio, "Fitting a straight line with errors on both coordinates," Bull. d'Inf. du Cent. Donnees Stellaires **35**, 191 (1988).

[40]J. Forneris, V. Grilj, M. Jaksic et al., "Measurement and modelling of anomalous polarity pulses in a multi-electrode diamond detector," EPL **104**, 28005 (2013).

[41]T. Hastie, R. Tibshirani, and J. Friedman, The Elements of Statistical Learning, Springer Series in Statistics (Springer, 2009).

[42]K. Höflich, G. Hobler, F. Allen et al., "Roadmap for focused ion beam technologies," Appl. Phys. Rev. **10**(4), 041311 (2023).

[43]M. Titze, H. Beyon, A. Flores et al., "In situ ion counting for improved implanted ion error rate and silicon vacancy yield uncertainty," Nano Lett. **22**, 3212–3218 (2022).

[44]J. L. Pacheco, M. Singh, D. L. Perry et al., "Ion implantation for deterministic single atom devices," Rev. Sci. Instrum. **88**(12), 123301 (2017).

[45]D. N. Jamieson, W. I. L. Lawrie, S. G. Robson *et al.*, "Deterministic doping," Mater. Sci. Semicond. Process. **62**, 23–30 (2017).

[46]S. Pezzagna, D. Rogalla, D. Wildanger *et al.*, "Creation and nature of optical centres in diamond for single-photon emission-overview and critical remarks," New J. Phys. **13**, 035024 (2011).

[47]S. M. Eaton, J. P. Hadden, V. Bharadwaj *et al.*, "Quantum micro–nano devices fabricated in diamond by femtosecond laser and ion irradiation," Adv. Quantum Technol. **2**(5-6), 1900006 (2019).

[48]S. G. Robson, P. Racke, A. M. Jakob *et al.*, "Near-surface electrical characterization of silicon electronic devices using focused keV-range ions," Phys. Rev. Appl. **18**(3), 034037 (2022).

[49]F. Dolde, H. Fedder, M. W. Doherty *et al.*, "Electric-field sensing using single diamond spins," Nat. Phys. **7**, 459–463 (2011).

[50]P. Siyushev, M. Nesladek, E. Bourgeois *et al.*, "Photoelectrical imaging and coherent spin-state readout of single nitrogen-vacancy centers in diamond," Science **363**, 728 (2019).

13 June 2024 07:44:34